


Article

Optimization of Ca–Al–Mn–Si Substitution Level for Enhanced Magnetic Properties of M-Type Sr-Hexaferrites for Permanent Magnet Application

Jun-Pyo Lim, Eel-Ho Yun and Young-Min Kang * 

Department of Materials Science & Engineering, Korea National University of Transportation,
Chungju 27469, Republic of Korea

* Correspondence: ymkang@ut.ac.kr

Abstract: Enhanced hard magnetic properties were achieved in M-type hexaferrite by optimizing the substitution levels of Mn, Al, and Si for Fe, and Ca for Sr within $\text{SrFe}_{12}\text{O}_{19}$. The addition of Al–Si–Mn effectively controlled crystallite growth, resulting in an increased coercivity (H_C), while causing a decrease in the remanent magnetization ($4\pi M_r$). A higher Ca content exhibited a trend of increasing the sintered density but decreasing the $4\pi M_r$ and H_C . The optimized composition, considering both the $4\pi M_r$ and H_C , was determined to be $\text{Sr}_{0.8}\text{Ca}_{0.2}\text{Fe}_{10.2}\text{Mn}_{0.1}\text{Al}_{0.2}\text{Si}_{0.1}\text{O}_{19-d}$, with a sintered density of 4.84 g/cm^3 , $4\pi M_r = 2.22 \text{ kG}$, and $H_C = 5.10 \text{ kOe}$. This result demonstrates the achievement of isotropic magnets with controlled crystal growth and densification without additional sintering additives. This development is promising, as this enhancement could be achieved without the use of cobalt, an expensive but essential ingredient in high-performance permanent magnets.

Keywords: M-type hexaferrites; cation substitution; coercivity; saturation magnetization; permanent magnet



Citation: Lim, J.-P.; Yun, E.-H.; Kang, Y.-M. Optimization of Ca–Al–Mn–Si Substitution Level for Enhanced Magnetic Properties of M-Type Sr-Hexaferrites for Permanent Magnet Application. *Appl. Sci.* **2023**, *13*, 12708. <https://doi.org/10.3390/app132312708>

Academic Editor: Evangelos Hristoforou

Received: 19 October 2023

Revised: 6 November 2023

Accepted: 15 November 2023

Published: 27 November 2023



Copyright: © 2023 by the authors. Licensee MDPI, Basel, Switzerland. This article is an open access article distributed under the terms and conditions of the Creative Commons Attribution (CC BY) license (<https://creativecommons.org/licenses/by/4.0/>).

1. Introduction

M-type hexaferrites (M-hexaferrites) with the chemical formula $(\text{Ba,Sr})\text{Fe}_{12}\text{O}_{19}$ are utilized as permanent magnet materials due to their strong c axis magnetocrystalline anisotropy (MCA) and sufficient saturation magnetization (M_S) [1,2]. Ferrite magnets are widely employed in various applications such as automotive, household appliances, and industrial equipment, including motors, compressors, transformers, and speakers, owing to their ease of fabrication under atmospheric conditions, excellent chemical stability, and cost-effectiveness. Ferrite magnets account for approximately 85% of the total mass of permanent magnets used worldwide [3], underscoring the economic and industrial significance of developing the advanced characteristics of M-hexaferrites.

Research efforts have been extensively conducted to enhance intrinsic magnetic properties, such as M_S and MCA, by substituting various ions in $\text{SrFe}_{12}\text{O}_{19}$ or $\text{BaFe}_{12}\text{O}_{19}$ [2,4–25]. In some cases, the selective substitution of non-magnetic elements like Zn for Fe's down-spin sites has led to an improved M_S in M-hexaferrites [4–8]. However, this has also resulted in a decrease in the MCA, leading to a reduction coercivity (H_C), and these materials have not been widely adopted as high-performance permanent magnets. On the other hand, M-hexaferrites with the simultaneous substitution of La–Co have been developed and used as high-performance permanent magnets [9–14]. In these cases, the substitution does not decrease the M_S while significantly increasing the MCA. An intriguing observation here is that when La^{3+} – Co^{2+} ions are simultaneously substituted for Sr^{2+} – Fe^{3+} ions in $\text{SrFe}_{12}\text{O}_{19}$, the MCA of M-hexaferrite significantly increases without a significant reduction in the M_S . However, when La or Co is substituted individually, such a remarkable improvement in characteristics cannot be achieved. Furthermore, when Co^{2+} – Ti^{4+} ions are substituted simultaneously for Fe^{3+} ions, there is an opposite trend, where MCA decreases as the substitution

level increases [26], in contrast to the substitution with $\text{La}^{3+}\text{-Co}^{2+}$. Therefore, research has extensively focused on the combinations of various substituting elements to enhance magnetic characteristics. Despite numerous studies, manufacturing high-performance ferrite magnets has remained challenging, and more effective results than the substitution of $\text{La}^{3+}\text{-Co}^{2+}$ have not been achieved. Since the cost of Co is significantly higher than that of other elements, developing cation substitution compositions that reduce or completely eliminate the need for Co is of paramount importance.

Recent advances in the field of hard magnetic materials have shown significant improvements in hexaferrite nanomagnets prepared using sol–gel-based methods [12,27,28]. These studies have demonstrated the attainment of a substantial H_C exceeding 6 kOe, primarily due to the nanocrystallization of hexaferrite grains. It is well-established that the coercivity of a single grain (h_C) increases as its size decreases, reaching the upper limit defined by the critical grain diameter for a single domain (d_{cri}). This phenomenon exhibits a reciprocal dependence on the grain size (d), expressed by the following equation [29]:

$$h_C = d_{cri} / d^{1.08} \quad (1)$$

However, when considering the practical application of sintered magnets, a method capable of mass production through solid-state reaction processes becomes imperative, as opposed to chemical synthesis methods like those of sol–gels.

Even when the magnetic properties of M-hexaferrite, such as the M_S and MCA, are improved through cation substitution during the calcination powder stage, these properties often deteriorate again due to the influence of sintering additives during the sintering process. Therefore, it is crucial to develop cation substitution compositions while considering the impact of sintering additives. Commonly used sintering additives, such as SiO_2 , play a significant role in controlling crystalline grain growth. However, during high-temperature sintering, Si can infiltrate the M-hexaferrite lattice, leading to a tendency to reduce magnetic properties like M_S [13,22]. Additionally, sintering additives like CaO and CaCO_3 promote grain growth and densification during sintering and can also affect the magnetic properties of M-hexaferrites when substituting for Sr or Fe sites [7,16,21–23].

In this study, our objective was to develop sintered magnets with improved magnetic properties, all while avoiding the use of sintering additives. To achieve this, we designed compositions such as $\text{Sr}_{0.8}\text{Ca}_{0.2}\text{Fe}_{12-3x}\text{Mn}_x\text{Al}_x\text{Si}_x\text{O}_{19-d}$, which incorporate essential elements like Si and Ca, known for their role in controlling grain growth and densification during sintering. Our choice of Mn as a dopant is due to its close similarity in size to Fe, and previous research has demonstrated that even small amounts of Mn substitution can enhance magnetic properties, such as the M_S [5–7,21–23]. We systematically adjusted the doping levels of Mn, Al, and Ca during the optimization process. In this composition formula, we represent the oxygen content as O_{19-d} , maintaining the charge balance between cations and oxygen ions. The substitution of Al and Si serves a function akin to sintering additives, effectively suppressing grain growth. In our previous research, we effectively controlled grain growth using only Si as an element [22,23]. However, in this study, we can expect to achieve an even better H_C with the combined action of Al and Si. When combined with the magnetic element Mn, we anticipated improvements in the magnetic properties at the optimal composition. Our goal was to identify the ideal substitution levels to enhance the magnetic characteristics. We conducted a comprehensive analysis of the crystalline phase, microstructure, and magnetic properties resulting from these substitutions, ultimately yielding a composition with cation substitutions well-suited for use as a ferrite permanent magnet.

2. Materials and Methods

To synthesize M-type Sr-hexaferrites with the cationic composition ratios of $\text{Sr}_{0.8}\text{Ca}_{0.2}\text{Fe}_{11-3x}\text{Mn}_x\text{Al}_x\text{Si}_x$, $\text{Sr}_{0.8}\text{Ca}_{0.2}\text{Fe}_{10.7-x-y}\text{Mn}_{0.1+x}\text{Al}_{0.1+y}\text{Si}_{0.1}$, $\text{Sr}_{0.7+z}\text{Ca}_{0.3-z}\text{Fe}_{10.2}\text{Mn}_{0.1}\text{Al}_{0.2}\text{Si}_{0.1}$, and $\text{Sr}_{0.7+z}\text{Ca}_{0.3-z}\text{Fe}_{9.7}\text{Mn}_{0.1}\text{Al}_{0.2}\text{Si}_{0.1}$ ($0 \leq x, y, z \leq 0.2$), a solid-state reaction method was employed. Setting the atomic ratio of [Sr-site]/[Fe-site] in the chemical formula

to 11 instead of 12 was based on the experimental results from previous research [5,6], aiming to suppress the formation of the secondary phase of Fe_2O_3 . Powders of Fe_2O_3 (99%, industrial use, Pohang, South Korea), SrCO_3 (99.9%, Kojundo Chemical, Sakado, Japan), CaCO_3 (98%, Showa chemical, Minato, Japan), Co_3O_4 (98%, Top new energy tech. Co., Xiamen, China), MnCO_3 (99.9%, Kojundo Chemical, Sakado, Japan), La_2O_3 (Sigma-Aldrich, 99.9%, St. Louis, MO, USA), and SiO_2 (99.5%, JK Silica Co., Shaxian, China) were weighed according to the cationic composition ratios. The weighed powders were mixed with distilled water in sample containers (Nalgene) and subjected to wet ball milling at 120 rpm for 20 h using zirconia balls. The fully dried powders were placed in alumina crucibles and calcined at 1100 °C for 4 h in an atmospheric electric furnace. After calcination, the powders were crushed, followed by a second 24 h wet milling. The milled powders were then dried and sieved through a 200 mesh sieve. A total of 5 g of the sieved powder was placed into a disk-shaped mold (20 mm diameter) and molded under a pressure of 0.3 tons. The molded samples were then sintered in an electric furnace under atmospheric conditions at 1210 °C for 2 h. During the ramp-up and ramp-down phases of the heating process, the furnace temperature was controlled at a rate of 5 °C/min, while natural cooling (furnace cooling) was employed during the cooling phase.

The density of the samples was calculated from the external dimensions and mass of the sintered disk-shaped samples. For phase analysis, the sintered samples were powdered, and X-ray diffraction (XRD) analysis was performed using an X-ray diffractometer (D8 Advance, Bruker, Karlsruhe, Germany) with $\text{Cu K}\alpha$ radiation ($\lambda = 0.154056$ nm). For microstructure observation, the fractured surface of the sintered samples were examined using a field emission scanning electron microscope (FE-SEM, JSM-7610F, JEOL, Tokyo, Japan). Magnetic properties were characterized by measuring the M-H curves of the sintered samples using a B-H loop tracer (BH-5501, Denshijiki Industry, Tokyo, Japan). The demagnetization curves in the second quadrant, measured by applying a maximum magnetic field of 25 kOe and then gradually decreasing the magnetic field, are presented.

3. Results and Discussion

3.1. Crystalline Structure and Microstructure Analysis

Figure 1a–d present the XRD patterns of the M-hexaferrite samples synthesized in this study in four series, based on different cationic compositions. All the samples were obtained through calcination at 1100 °C in an air atmosphere and sintering at 1210 °C. The XRD patterns of the M-hexaferrite phase were indexed based on the International Center for Diffraction Data (ICDD) with the pdf search number SrM: 00-033-1340. For some samples, the peak positions of the secondary phase Fe_2O_3 (ICDD, 33-0664) that occurred in certain samples are also indicated. In Figure 1a, the formation of the M-hexaferrite phase in $\text{Sr}_{0.8}\text{Ca}_{0.2}\text{Fe}_{11-3x}\text{Mn}_x\text{Al}_x\text{Si}_x\text{O}_{19-d}$, where 20% of Sr in the basic composition of M-hexaferrite $\text{SrFe}_{12}\text{O}_{19}$ is substituted with Ca, and Fe is simultaneously substituted with Mn, Al, and Si, is shown. For $x = 0$ and 0.05, a pure M-hexaferrite phase is formed, whereas for $x = 0.1$, a small Fe_2O_3 peak is observed, and as x increases to 0.15 and 0.2, the Fe_2O_3 peak becomes significantly more pronounced. For the $x = 0$ composition, it can be observed that the 00l peaks, such as 006, 008, and 0014, are significantly higher compared to the other compositions. This result can be explained as follows: in samples with large grain growth, wide plate-like hexaferrite grains are abundant even in the powdered state. During the packing of the powder into the sample holder for the XRD measurements, the c-axes of each grain align perpendicular to the sample holder's surface. This phenomenon has been reported in previous studies on hexaferrites [7,16,23]. Figure 1b shows the XRD patterns of $\text{Sr}_{0.8}\text{Ca}_{0.2}\text{Fe}_{10.7-3x}\text{Mn}_{0.1+x}\text{Al}_{0.1+y}\text{Si}_{0.1}\text{O}_{19-d}$ ($0 \leq x, y \leq 0.1$), in which either of the Mn and Al substitution levels are increased from one of the first series samples, $\text{Sr}_{0.8}\text{Ca}_{0.2}\text{Fe}_{10.7}\text{Mn}_{0.1}\text{Al}_{0.1}\text{Si}_{0.1}\text{O}_{19-d}$ ($x = 0$). All four samples show the presence of a secondary phase Fe_2O_3 in small amounts. Figure 1c,d display the XRD patterns of two series samples, $\text{Sr}_{0.7+z}\text{Ca}_{0.3-z}\text{Fe}_{10.2}\text{Mn}_{0.1}\text{Al}_{0.2}\text{Si}_{0.11}\text{O}_{19-d}$ and $\text{Sr}_{0.7+z}\text{Ca}_{0.3-z}\text{Fe}_{9.7}\text{Mn}_{0.1}\text{Al}_{0.2}\text{Si}_{0.11}\text{O}_{19-d}$ ($z = 0.05, 0.1, 0.15, 0.2$). In these samples, the

ratio of Sr:Ca is varied and the Fe content in the formula is reduced from 10.6 to 10.2 and 9.7, respectively. All eight samples in Figure 1c,d are single-phase M-hexaferrites. The phases of each composition confirmed from the XRD analysis are summarized in Table 1.

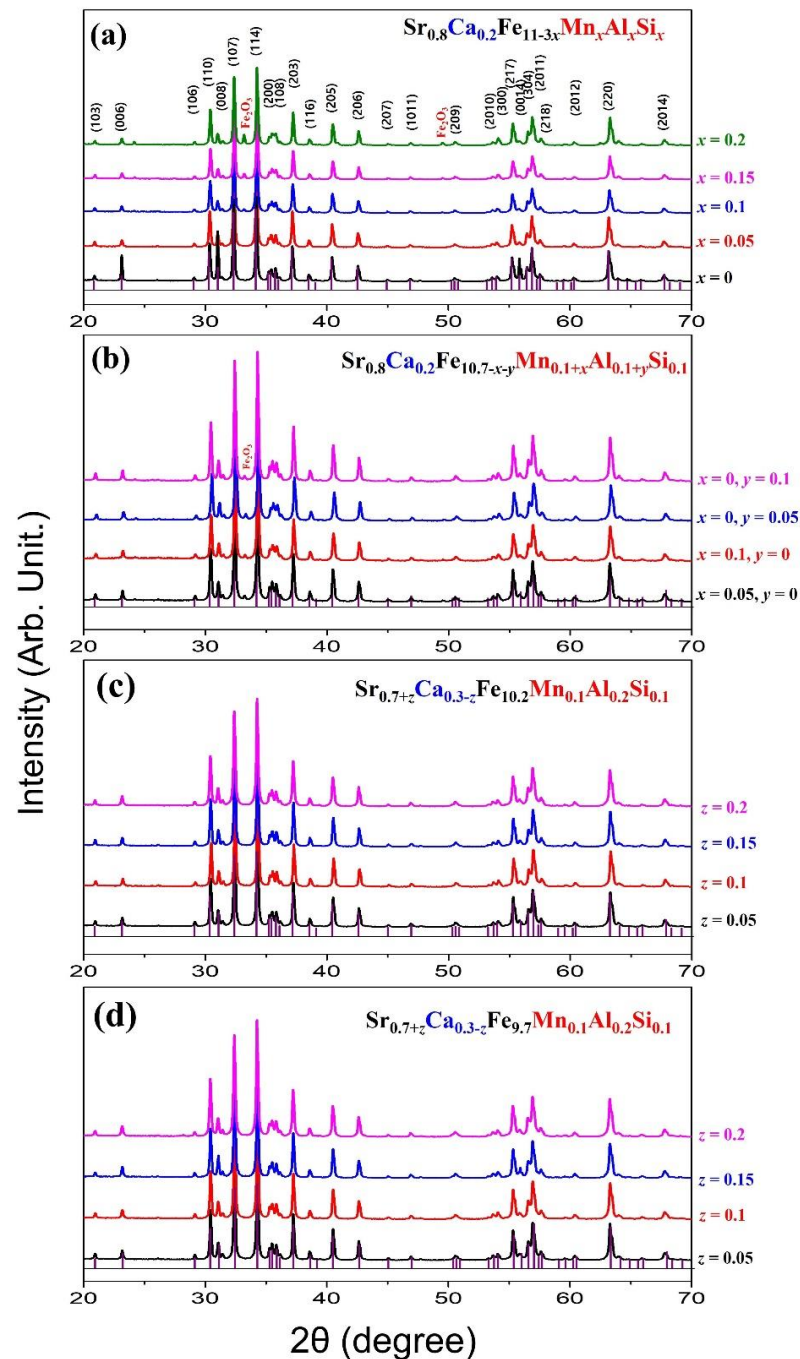


Figure 1. XRD patterns of M-hexaferrites, (a) $\text{Sr}_{0.8}\text{Ca}_{0.2}\text{Fe}_{11-3x}\text{Mn}_x\text{Al}_x\text{Si}_x\text{O}_{19-d}$, (b) $\text{Sr}_{0.8}\text{Ca}_{0.2}\text{Fe}_{10.7-3x}\text{Mn}_{0.1+x}\text{Al}_{0.1+y}\text{Si}_{0.1}\text{O}_{19-d}$, (c) $\text{Sr}_{0.7+z}\text{Ca}_{0.3-z}\text{Fe}_{10.2}\text{Mn}_{0.1}\text{Al}_{0.2}\text{Si}_{0.1}\text{O}_{19-d}$, (d) $\text{Sr}_{0.7+z}\text{Ca}_{0.3-z}\text{Fe}_{9.7}\text{Mn}_{0.1}\text{Al}_{0.2}\text{Si}_{0.1}\text{O}_{19-d}$ sintered at 1210 °C.

Table 1. Sample composition with substitution content (x, y, z), sintering temperature (T_S), cell volume (Vol), sintered sample density (ρ), saturation magnetization ($4\pi M_S$), and coercivity (H_C) of the sintered hexaferrite samples.

Cation Composition	x, y, z	XRD (Phase)	ρ (g/cm ³)	a (Å)	c (Å)	V (Å ³)	$4\pi M_r$ (kG)	H_C (kOe)
Sr _{0.8} Ca _{0.2} Fe _{11–3x} Mn _x Al _x Si _x	$x = 0$	M	4.96	5.881	23.05	690.3	2.57	2.80
	$x = 0.05$	M	4.89	5.881	23.04	690.0	2.30	3.59
	$x = 0.1$	M+Fe ₂ O ₃	4.81	5.875	23.04	688.8	2.25	4.72
	$x = 0.15$	M+Fe ₂ O ₃	4.90	5.870	23.04	687.1	2.20	4.76
	$x = 0.2$	M+Fe ₂ O ₃	4.90	5.871	23.04	687.7	2.04	4.90
Sr _{0.8} Ca _{0.2} Fe _{10.7–x–y} Mn _{0.1+x} Al _{0.1+y} Si _{0.1}	$x = 0.05$	M+Fe ₂ O ₃	4.78	5.869	23.01	686.3	2.18	4.65
	$x = 0.1$	M+Fe ₂ O ₃	4.74	5.863	22.98	684.1	2.19	4.66
	$y = 0.05$	M+Fe ₂ O ₃	4.80	5.852	22.94	680.4	2.21	4.83
	$y = 0.1$	M+Fe ₂ O ₃	4.85	5.866	23.00	685.3	2.20	5.01
Sr _{0.7+z} Ca _{0.3–z} Fe _{10.2} Mn _{0.1} Al _{0.2} Si _{0.1}	$z = 0.05$	M	4.81	5.870	23.01	686.5	2.22	5.00
	$z = 0.1$	M	4.84	5.861	22.99	684.1	2.22	5.10
	$z = 0.15$	M	4.76	5.868	23.01	686.0	2.16	5.20
	$z = 0.2$	M	4.70	5.872	23.03	687.6	2.13	5.32
Sr _{0.7+z} Ca _{0.3–z} Fe _{9.7} Mn _{0.1} Al _{0.2} Si _{0.1}	$z = 0.05$	M	4.88	5.870	23.00	686.2	2.21	4.92
	$z = 0.1$	M	5.00	5.869	23.00	686.2	2.23	4.99
	$z = 0.15$	M	4.86	5.869	23.00	686.2	2.18	5.07
	$z = 0.2$	M	4.73	5.868	23.02	686.5	2.14	5.16

The error bar for ρ , $4\pi M_r$, H_C is $\pm 0.3\%$, $\pm 0.2\%$, $\pm 1\%$ of the original values, respectively.

Additionally, the lattice constants a , c , and the unit cell volume (V) were calculated from the XRD peaks and are presented in Table 1. The a and c are calculated from the values of d_{hkl} corresponding to the (107) and (114) peaks, according to the following equation:

$$d_{hkl} = \left\{ \frac{4(h^2 + hk + k^2)}{3a^2} + \frac{l^2}{c^2} \right\}^{-1/2} \quad (2)$$

where d_{hkl} is the interplanar spacing, and h, k , and l are the Miller indices. As the substitution level x increases, the unit cell volume generally decreases due to the smaller average ionic radii of Mn³⁺, Al²⁺, and Si⁴⁺ compared to Fe³⁺. Furthermore, since Sr²⁺ has a larger ionic radius than Ca²⁺, it could be expected that the unit cell volume would increase with increasing z . However, this trend is not observed in this experiment.

Figure 2a–e illustrate the changes in the microstructure with increasing x in sintered Sr_{0.8}Ca_{0.2}Fe_{11–3x}Mn_xAl_xSi_xO_{19–d} samples. The average grain size (D) was determined using a random intercept method applied to SEM micrographs and is presented in the lower right corner of each figure. Notably, when Mn–Al–Si substitutions are absent ($x = 0$), the average grain size is the largest, at $D = 2.23 \mu\text{m}$. With increasing x , there is a consistent trend of decreasing D . Given that the substitution of Mn–Al–Si does not significantly affect the MCA of M-hexaferrite, it can be explained that H_C is primarily dependent on D . As discussed earlier in Equation (1), the coercivity of an individual grain (h_C) exhibits an inverse relationship with its size (d), which can aptly account for these variations. The abnormally high intensity of the (001) plane peaks in the XRD pattern of the $x = 0$ sample (Figure 1a) is attributed to the growth of hexagonal plate-like crystals, which can be observed in Figure 2a. In Figure 2c–e, for samples with $x \geq 0.1$, a uniform grain size distribution is evident, with D ranging between 1.15 and 1.33 μm . In Figure 2f,g, when the Mn substitution level is increased to 0.15 and 0.2, a slight increase in D is observed. However, in Figure 2h,i, as the Al substitution level increases to 0.15 and 0.2, there is a slight tendency for D to decrease. The apparent density of the sintered samples for each composition is presented in Table 1.

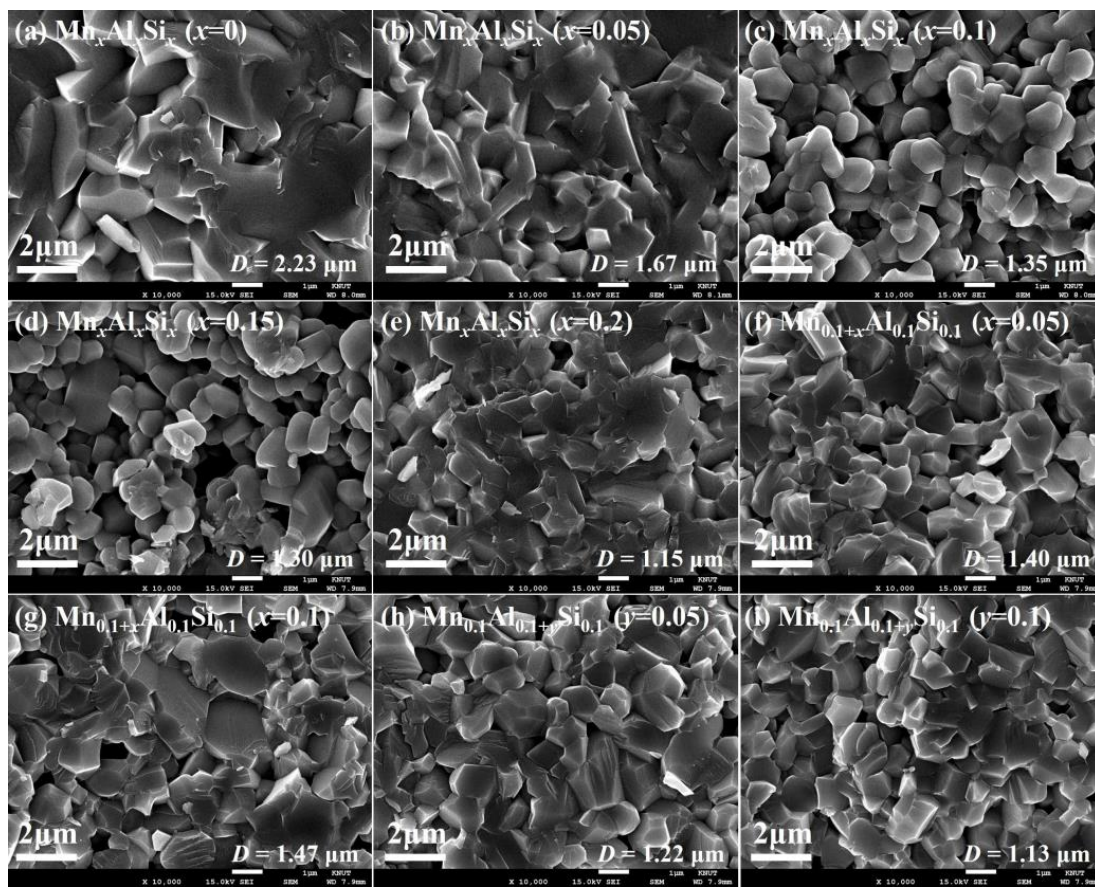


Figure 2. SEM micrographs of sintered (a–e) $\text{Sr}_{0.8}\text{Ca}_{0.2}\text{Fe}_{11-3x}\text{Mn}_x\text{Al}_x\text{Si}_x\text{O}_{19-d}$ with $x = 0, 0.05, 0.1, 0.15, 0.2$, and (f–i) $\text{Sr}_{0.8}\text{Ca}_{0.2}\text{Fe}_{10.7-3x}\text{Mn}_{0.1+x}\text{Al}_{0.1+y}\text{Si}_{0.1}\text{O}_{19-d}$ with $x, y = 0.05, 0.1$, sintered at 1210°C .

3.2. Magnetic Property Analysis

Figure 3a–d display the demagnetization curves ($4\pi\text{M-H}$) of samples for each composition in the four series. Additionally, to facilitate an easy assessment of the changes in the residual magnetization ($4\pi\text{M}_r$) and coercivity (H_C) of the samples obtained here, we have plotted them as a function of the substitution level x , y , and z in Figure 4a–e. The precise data values are provided in Table 1. In Figure 3a, it can be observed that the demagnetization curves vary significantly with respect to the Mn–Al–Si substitution level, x . As x increases, $4\pi\text{M}_r$ decreases, while H_C shows an increasing trend. When there is no secondary phase, $4\pi\text{M}_r$ can be expressed in terms of the M_S , sintered density (ρ), and squareness (S), as follows [7,23]:

$$4\pi\text{M}_r = M_S \cdot \rho \cdot S \quad (3)$$

here, $4\pi\text{M}_r$ is the remanent magnetization in Gauss units, M_S is the saturation magnetization in emu/g unit, ρ is the sintered density in g/cm^3 , and S represents the squareness, which is a measure of the degree of alignment along the c axis in the crystallites. It can be expressed as the ratio of the remanent magnetization to saturation magnetization ($S = \text{M}_r/\text{M}_S$). The saturation magnetization in Gauss units ($4\pi\text{M}_S$) can be estimated as twice the value of $4\pi\text{M}_r$ in the case of an isotropic magnet, where the crystalline grains are randomly oriented. Since the M_S of Sr M-hexaferrite in the units of emu/g is known to be 72 emu/g [2,3], the theoretical $4\pi\text{M}_S$ can be approximately 4600 G . In this case, for a perfectly isotropic magnet with a theoretical density of $5.1 \text{ g}/\text{cm}^3$, the $4\pi\text{M}_r$ would be around 2300 G .

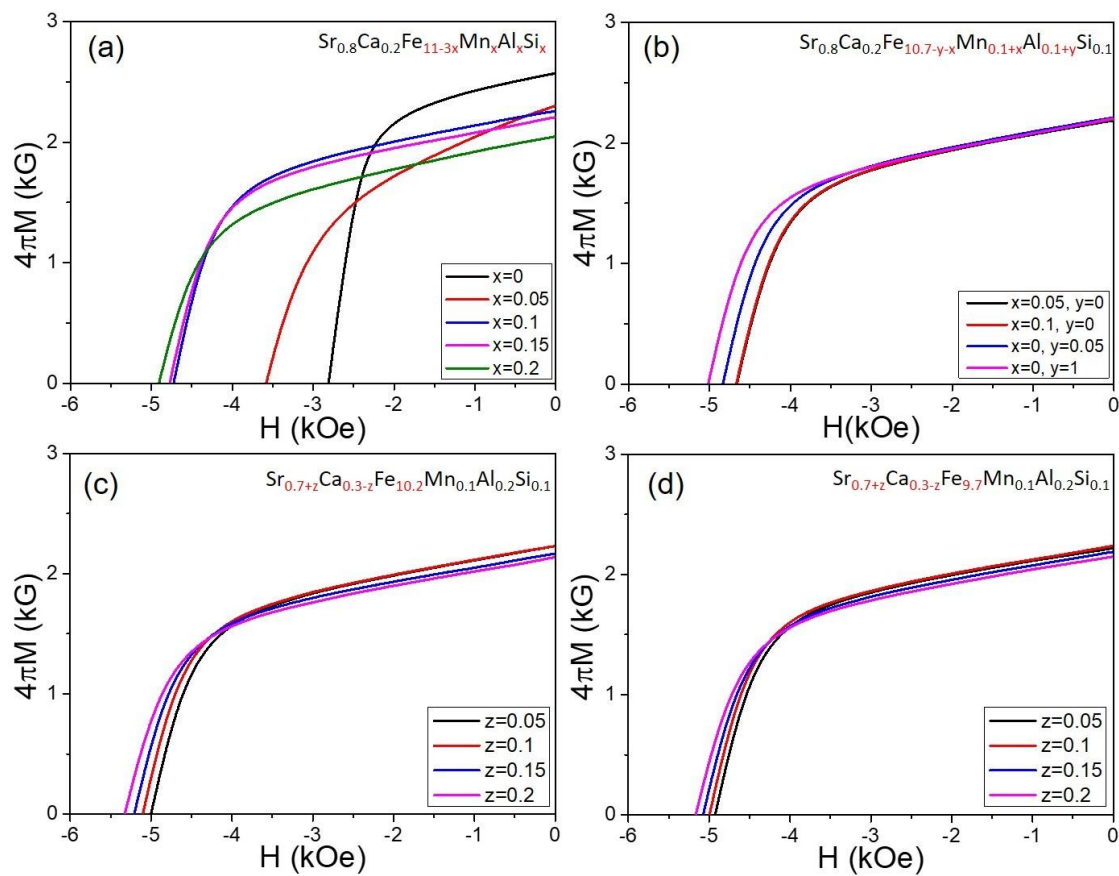


Figure 3. Demagnetization curves of hexaferrite samples, (a) $\text{Sr}_{0.8}\text{Ca}_{0.2}\text{Fe}_{11-3x}\text{Mn}_x\text{Al}_x\text{Si}_x\text{O}_{19-d}$, (b) $\text{Sr}_{0.8}\text{Ca}_{0.2}\text{Fe}_{10.7-3x}\text{Mn}_{0.1+x}\text{Al}_{0.1+y}\text{Si}_{0.1}\text{O}_{19-d}$, (c) $\text{Sr}_{0.7+z}\text{Ca}_{0.3-z}\text{Fe}_{10.2}\text{Mn}_{0.1}\text{Al}_{0.2}\text{Si}_{0.1}\text{O}_{19-d}$, and (d) $\text{Sr}_{0.7+z}\text{Ca}_{0.3-z}\text{Fe}_{9.7}\text{Mn}_{0.1}\text{Al}_{0.2}\text{Si}_{0.1}\text{O}_{19-d}$ ($0 \leq x, y, z \leq 0.2$).

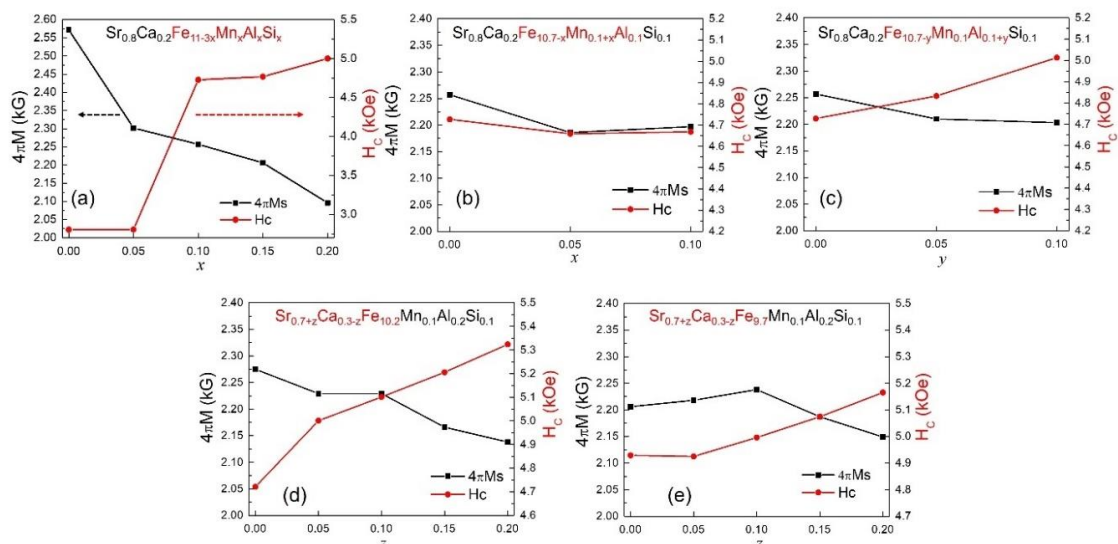


Figure 4. (a–e) Dependence of $4\pi M_r$ and H_c on substitution compositions (x, y, z) of the M-hexaferrites.

In Figure 3a, the $x = 0$ sample exhibits a significantly higher $4\pi M_r$ of 2570 G than the expected $4\pi M_r$ for a perfectly isotropic magnet. This can be attributed to some degree to the c axis alignment in the crystallites. Based on the size and shape of the crystalline grains observed in the SEM images in Figure 2a, it can be inferred that the $x = 0$ sample maintains hexagonal plate-like crystallites even after secondary ball milling and exhibits

some *c* axis alignment after the molding process into disk shapes. The $x = 0.05$ sample shown in Figure 2b is also expected to show a weaker degree of *c* axis alignment for the same reasons. For samples with $x \geq 0.1$, as shown in Figure 3a, considering the size and shape of the crystallites from Figure 2c–e, they are expected to be nearly perfectly isotropic. Therefore, the $4\pi M_s$ for these samples can be roughly estimated as twice the value of the $4\pi M_r$. In these samples ($x \geq 0.1$), the crystalline grain size and distribution are uniform. In Figure 4a, it is noticeable that the H_C sharply increases at $x = 0.1$. Among the samples in the series presented in Figure 3a for $\text{Sr}_{0.8}\text{Ca}_{0.2}\text{Fe}_{11-3x}\text{Mn}_x\text{Al}_x\text{Si}_x\text{O}_{19-d}$, when considering both the $4\pi M_r$ and H_C values, it is concluded that the composition at $x = 0.1$, $\text{Sr}_{0.8}\text{Ca}_{0.2}\text{Fe}_{10.7}\text{Mn}_{0.1}\text{Al}_{0.1}\text{Si}_{0.1}\text{O}_{19-d}$, exhibits the most optimized results for permanent magnet applications. Additionally, there is still room for improvement in $4\pi M_r$ through improving the sintering density and removing the second phase Fe_2O_3 .

Figure 3b shows the demagnetization curves of $\text{Sr}_{0.8}\text{Ca}_{0.2}\text{Fe}_{10.7-x-y}\text{Mn}_{0.1+x}\text{Al}_{0.1+y}\text{Si}_{0.1}\text{O}_{19-d}$ ($0 \leq x, y \leq 0.1$), in which either of the Mn and Al substitution levels are increased from the first optimized composition in Figure 3a, $\text{Sr}_{0.8}\text{Ca}_{0.2}\text{Fe}_{10.7}\text{Mn}_{0.1}\text{Al}_{0.1}\text{Si}_{0.1}\text{O}_{19-d}$ ($x = 0$). Among the four demagnetization curves, it can be observed that there is a significant improvement in H_C when adding Al content with $y = 0.1$, while the $4\pi M_s$ values remain relatively consistent. In Figure 4b,c, one can easily compare the relative magnitude of the $4\pi M_r$ and H_C values for these samples. Therefore, based on these results, the second optimized composition can be derived as $\text{Sr}_{0.8}\text{Ca}_{0.2}\text{Fe}_{10.6}\text{Mn}_{0.1}\text{Al}_{0.2}\text{Si}_{0.1}\text{O}_{19-d}$.

The XRD phase analysis results presented in Figure 1 show that all four samples shown in Figure 3b contain a secondary phase of Fe_2O_3 . Therefore, the Fe content in the chemical formula was reduced from the stoichiometric composition of 10.6 to 10.2 and 9.7, respectively, while the Sr:Ca ratio was slightly adjusted. The results for these two series of compositions, $\text{Sr}_{0.7+z}\text{Ca}_{0.3-z}\text{Fe}_{10.2}\text{Mn}_{0.1}\text{Al}_{0.2}\text{Si}_{0.1}\text{O}_{19-d}$ and $\text{Sr}_{0.7+z}\text{Ca}_{0.3-z}\text{Fe}_{9.7}\text{Mn}_{0.1}\text{Al}_{0.2}\text{Si}_{0.1}\text{O}_{19-d}$ ($z = 0, 0.05, 0.1, 0.15, 0.2$), are presented in Figures 3c and 4d, respectively. The changes in the $4\pi M_r$ and H_C values with respect to z are also plotted in Figure 4d,e. In both cases, an increase in z (corresponding to a decrease in the Ca content) leads to an increase in H_C , and a decrease in the $4\pi M_s$ values, roughly. This is related to the tendency of the Ca content to promote grain growth. Furthermore, the composition with $z = 0.1$, which corresponds to Sr:Ca = 0.8:0.2, exhibited the highest sintered density. Considering both the $4\pi M_r$ and H_C values, the composition with the Fe content at 10.2 and $z = 0.1$ (i.e., $\text{Sr}_{0.8}\text{Ca}_{0.2}\text{Fe}_{10.2}\text{Mn}_{0.1}\text{Al}_{0.2}\text{Si}_{0.1}\text{O}_{19-d}$) can be derived as the final optimized composition.

In ferrite magnets, it is well-known that there is a trade-off relationship between $4\pi M_r$ and H_C . To confirm this trend observed in the five series of compositions in this study, the $4\pi M_r$ and H_C of all the samples were plotted as points in a two-dimensional plane (x, y) and presented in Figure 5. Each series of samples is represented by shapes and colors of the same type. Furthermore, a trend line with a consistent slope from the bottom-left to the top-right are drawn from the coordinate points of each series, helping distinguish the positions of the points. A specific point that trends towards the upper-right direction indicates superior permanent magnet properties. In the first series, $\text{Sr}_{0.8}\text{Ca}_{0.2}\text{Fe}_{11-3x}\text{Mn}_x\text{Al}_x\text{Si}_x\text{O}_{19-d}$ ($x = 0, 0.05, 0.1, 0.15, 0.2$), it is confirmed that the composition with $x = 0.1$ is positioned most towards the upper-right direction. In the second series, $\text{Sr}_{0.8}\text{Ca}_{0.2}\text{Fe}_{10.7-3x}\text{Mn}_{0.1+x}\text{Al}_{0.1+y}\text{Si}_{0.1}\text{O}_{19-d}$, when additional Al substitution ($y = 0.1$) is applied, it is observed that this composition is located most towards the upper-right direction. Finally, in the two series where the Sr:Ca ratio is adjusted, $\text{Sr}_{0.7+z}\text{Ca}_{0.3-z}\text{Fe}_{10.2}\text{Mn}_{0.1}\text{Al}_{0.2}\text{Si}_{0.1}\text{O}_{19-d}$, $\text{Sr}_{0.7+z}\text{Ca}_{0.3-z}\text{Fe}_{9.7}\text{Mn}_{0.1}\text{Al}_{0.2}\text{Si}_{0.1}\text{O}_{19-d}$ ($z = 0, 0.05, 0.1, 0.15, 0.2$), it is again confirmed that the composition with $z = 0.1$ is positioned most towards the upper-right direction. This analysis reaffirms the validity of the step-by-step optimization process to derive the final optimized composition for the permanent magnet properties in each series of compositions.

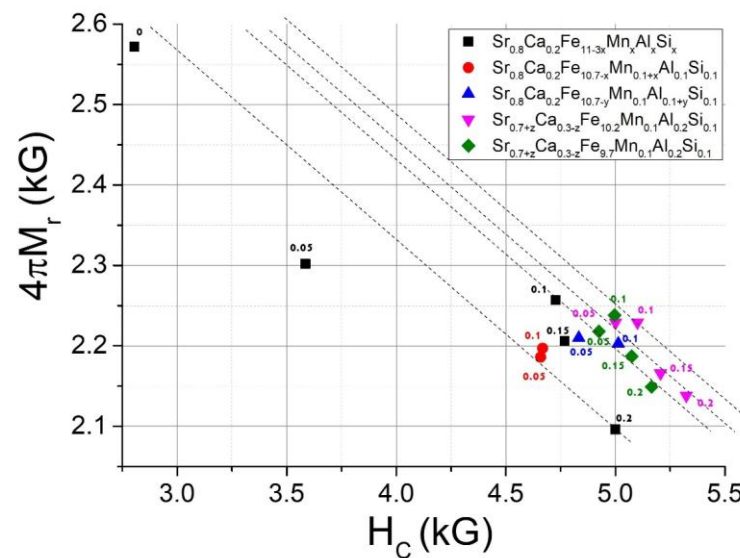


Figure 5. Plot of $4\pi M_r$ and H_C of the sintered hexaferrite samples.

4. Conclusions

In this study, M-hexaferrites ($\text{SrFe}_{12}\text{O}_{19}$) with Mn–Al–Si and Ca substitutions were fabricated by a solid-state reaction, and their crystalline structure, microstructure, and magnetic properties were evaluated. The goal was to optimize the cation substitution composition for permanent magnets by considering two key magnetic properties, $4\pi M_r$ and H_C . It was also planned to achieve grain growth inhibition and densification through the compositional control of the initial raw materials without adding separate sintering additives. Initially, in the composition $\text{Sr}_{0.8}\text{Ca}_{0.2}\text{Fe}_{11-3x}\text{Mn}_x\text{Al}_x\text{Si}_x\text{O}_{19-d}$, we obtained a significant improvement in the magnetic properties, with a well-controlled grain size at $x = 0.1$, that is, $\text{Sr}_{0.8}\text{Ca}_{0.2}\text{Fe}_{10.7}\text{Mn}_{0.1}\text{Al}_{0.1}\text{Si}_{0.1}\text{O}_{19-d}$, resulting in an increased H_C . From there, we increased the Mn and Al content step by step in the composition $\text{Sr}_{0.8}\text{Ca}_{0.2}\text{Fe}_{10.7-x-y}\text{Mn}_{0.1+x}\text{Al}_{0.1+y}\text{Si}_{0.1}\text{O}_{19-d}$, and it was observed that the composition with $x = 0$ and $y = 0.1$ exhibited the best magnetic properties ($4\pi M_r = 2.20$ kG, $H_C = 5.01$ kOe). However, it was noted that Fe_2O_3 existed in trace amounts as a secondary phase. In the next step, the Fe content was reduced, and the Sr to Ca ratio was adjusted in two compositions, $\text{Sr}_{0.7+z}\text{Ca}_{0.3-z}\text{Fe}_{10.2}\text{Mn}_{0.1}\text{Al}_{0.2}\text{Si}_{0.1}\text{O}_{19-d}$ and $\text{Sr}_{0.7+z}\text{Ca}_{0.3-z}\text{Fe}_{9.7}\text{Mn}_{0.1}\text{Al}_{0.2}\text{Si}_{0.1}\text{O}_{19-d}$ ($z = 0.05, 0.1, 0.15, 0.2$), resulting in the final optimized composition, $\text{Sr}_{0.8}\text{Ca}_{0.2}\text{Fe}_{10.2}\text{Mn}_{0.1}\text{Al}_{0.2}\text{Si}_{0.1}\text{O}_{19-d}$. This sample exhibited a sintered density $\rho = 4.84$ g/cm³, $4\pi M_r = 2.22$ kG, and $H_C = 5.10$ kOe. This result is achieved in a completely isotropic magnet with no crystal orientation. Through the implementation of high-energy ball milling to obtain finer powders, which enhances the sintering density, and the application of a magnetic field pressing to align the c axis crystal orientation, there is potential to develop an anisotropic magnet with an $M_r/M_s = 0.95$ and $\rho = 5.0$ g/cm³ [21–23]. Based on these assumptions, we anticipate that further process optimization will enable the same composition of anisotropic magnets to achieve $4\pi M_r = 4.40$ kG, $H_C = 4.8$ kOe, and a maximum energy product (BH_{\max}) of 4.65 M·G·Oe. Overall, these results are highly promising, particularly as they were achieved without the need for cobalt, a costly material typically essential for high-performance ferrite magnets.

Author Contributions: Conceptualization, Y.-M.K.; funding acquisition, Y.-M.K.; investigation, Y.-M.K.; methodology, J.-P.L. and E.-H.Y.; project administration, Y.-M.K.; software, J.-P.L. and E.-H.Y.; supervision, Y.-M.K.; writing—original draft, Y.-M.K. All authors have read and agreed to the published version of the manuscript.

Funding: This research was supported by “Regional Innovation Strategy (RIS)” through the National Research Foundation of Korea (NRF), funded by the Ministry of Education (MOE) (2021RIS-001).

Institutional Review Board Statement: Not applicable.

Informed Consent Statement: Not applicable.

Data Availability Statement: The data presented in this study are available on request from the corresponding author. The data are not publicly available due to privacy.

Acknowledgments: The authors are also grateful to Union Materials Corp. in Pohang, South Korea, for the support with the raw materials for the magnet fabrication.

Conflicts of Interest: The authors declare no conflict of interest.

References

- Went, J.; Rathenau, G.; Gorter, E.; Oosterhout, G.V. Ferroxidure, a class of new permanent magnet materials. *Philips Tech. Rev.* **1952**, *13*, 194–208.
- Pullar, R.C. Hexagonal ferrites: A review of the synthesis, properties and applications of hexaferrite ceramics. *Prog. Mater. Sci.* **2012**, *57*, 1191–1334. [\[CrossRef\]](#)
- Granados-Miralles, C.; Jenuš, P. On the potential of hard ferrite ceramics for permanent magnet technology—A review on sintering strategies. *J. Phys. D Appl. Phys.* **2021**, *54*, 303001. [\[CrossRef\]](#)
- Bai, J.; Liu, X.; Xie, T.; Wei, F.; Yang, Z. The effects of La–Zn substitution on the magnetic properties of Sr-magnetoplumbite ferrite nano-particles. *Mater. Sci. Eng. B* **2000**, *68*, 182–185. [\[CrossRef\]](#)
- Kang, Y.-M.; Kwon, Y.-H.; Kim, M.-H.; Lee, D.-Y. Enhancement of magnetic properties in Mn–Zn substituted M-type Sr-hexaferrites. *J. Magn. Magn. Mater.* **2015**, *382*, 10–14. [\[CrossRef\]](#)
- Kang, Y.-M.; Moon, K.-S. Magnetic properties of Ce–Mn substituted M-type Sr-hexaferrites. *Ceram. Int.* **2015**, *41*, 12828–12834. [\[CrossRef\]](#)
- Moon, K.-S.; Kang, Y.-M. Structural and magnetic properties of Ca–Mn–Zn-substituted M-type Sr-hexaferrites. *J. Eur. Ceram. Soc.* **2016**, *36*, 3383–3389. [\[CrossRef\]](#)
- Huang, K.; Yu, J.; Zhang, L.; Xu, J.; Yang, Z.; Liu, C.; Wang, W.; Kan, X. Structural and magnetic properties of Gd–Zn substituted M-type Ba–Sr hexaferrites by sol-gel auto-combustion method. *J. Alloys Compd.* **2019**, *803*, 971–980. [\[CrossRef\]](#)
- Kools, F.; Morel, A.; Grössinger, R.; Le Breton, J.M.; Tenaud, P. LaCo-substituted ferrite magnets, a new class of high-grade ceramic magnets; intrinsic and microstructural aspects. *J. Magn. Magn. Mater.* **2002**, *242–245*, 1270–1276. [\[CrossRef\]](#)
- Ogata, Y.; Takami, T.; Kubota, Y. Development of La–Co Substituted Ferrite Magnets. *J. Jpn. Soc. Powder Powder Metall.* **2003**, *50*, 636–641. [\[CrossRef\]](#)
- Kobayashi, Y.; Hosokawa, S.; Oda, E.; Toyota, S. Magnetic properties and composition of Ca–La–Co M-type ferrites. *J. Jpn. Soc. Powder Powder Metall.* **2008**, *55*, 541–546. [\[CrossRef\]](#)
- Lee, J.; Lee, E.J.; Hwang, T.-Y.; Kim, J.; Choa, Y.-H. Anisotropic characteristics and improved magnetic performance of Ca–La–Co-substituted strontium hexaferrite nanomagnets. *Sci. Rep.* **2020**, *10*, 15929. [\[CrossRef\]](#) [\[PubMed\]](#)
- Moon, K.-S.; Yu, P.-Y.; Kang, Y.-M. Microstructure and magnetic properties of La–Ca–Co substituted M-type Sr-hexaferrites with controlled Si diffusion. *Appl. Sci.* **2020**, *10*, 7570. [\[CrossRef\]](#)
- Zhou, Y.; Jiang, T.; Xu, B.; Dong, Z.; Wu, J.; Zhang, M.; Chen, Y.; Zhong, S. Clean and economical preparation of Ca–La–Co substituted permanent ferrite magnet with ultrapure magnetite concentrate. *J. Alloys Compd.* **2023**, *956*, 170334. [\[CrossRef\]](#)
- Yasmin, N.; Mirza, M.; Muhammad, S.; Zahid, M.; Ahmad, M.; Awan, M.S.; Muhammad, A. Influence of samarium substitution on the structural and magnetic properties of M-type hexagonal ferrites. *J. Magn. Magn. Mater.* **2018**, *446*, 276–281. [\[CrossRef\]](#)
- Moon, K.-S.; Lim, E.-S.; Kang, Y.-M. Effect of Ca and La substitution on the structure and magnetic properties of M-type Sr-hexaferrites. *J. Alloys Compd.* **2019**, *771*, 350–355. [\[CrossRef\]](#)
- Almessiere, M.A.; Slimani, Y.; Güner, S.; van Leusen, J.; Baykal, A.; Kögerler, P. Effect of Nb³⁺ ion substitution on the magnetic properties of SrFe₁₂O₁₉ hexaferrites. *J. Mater. Sci. Mater. Electron.* **2019**, *30*, 11181–11192. [\[CrossRef\]](#)
- Todkar, G.B.; Kunale, R.A.; Kamble, R.N.; Batoo, K.M.; Ijaz, M.F.; Imran, A.; Hadi, M.; Raslan, E.H.; Shirsath, S.E.; Kadam, R.H. Ce–Dy substituted barium hexaferrite nanoparticles with large coercivity for permanent magnet and microwave absorber application. *J. Phys. D Appl. Phys.* **2021**, *54*, 294001. [\[CrossRef\]](#)
- Han, G.; Sui, R.; Yu, Y.; Wang, L.; Li, M.; Li, J.; Liu, H.; Yang, W. Structure and magnetic properties of the porous Al-substituted barium hexaferrites. *J. Magn. Magn. Mater.* **2021**, *528*, 167824. [\[CrossRef\]](#)
- Manglam, M.K.; Shukla, A.; Mallick, J.; Yadav, M.K.; Kumari, S.; Zope, M.; Kar, M. Enhancement of coercivity of M-type barium hexaferrite by Ho doping. *Mater. Today Proc.* **2022**, *59*, 149–152. [\[CrossRef\]](#)
- Yu, P.-Y.; Kim, M.-H.; Kang, Y.-M. Development of a high-performance ferrite magnet fabrication process without sintering additives. *Korean J. Met. Mater.* **2021**, *59*, 551–559. [\[CrossRef\]](#)
- Yoo, J.-Y.; Lee, K.-H.; Kang, Y.-M.; Yoo, S.-I. Enhancement of the magnetic properties in Si⁴⁺–Li⁺-substituted M-type hexaferrites for permanent magnets. *Appl. Sci.* **2022**, *12*, 12295. [\[CrossRef\]](#)
- Lim, J.-P.; Kang, M.-G.; Kang, Y.-M. Development of Multi-Cation-Doped M-Type Hexaferrite Permanent Magnets. *Appl. Sci.* **2023**, *13*, 295. [\[CrossRef\]](#)

24. Yu, X.; Wang, L.; Liu, R.; Zhou, N.; Xu, Z.; Gong, H.; Zhao, T.; Sun, J.; Hu, F.; Shen, B. Simultaneous improvement of coercivity and saturation magnetization of M-type strontium ferrite by $\text{Nd}^{3+}\text{-Co}^{2+}$ unequal co-substitution. *Ceram. Int.* **2023**, *49*, 10499–10505. [[CrossRef](#)]
25. Gholizadeh, A.; Banihashemi, V. Effects of Ca–Gd co-substitution on the structural, magnetic, and dielectric properties of M-type strontium hexaferrite. *J. Am. Ceram. Soc.* **2023**, *106*, 5351–5363. [[CrossRef](#)]
26. Thompson, S.; Shirtcliffe, N.J.; O’Keefe, E.S.; Appleton, S.; Perry, C.C. Synthesis of $\text{SrCo}_x\text{Ti}_x\text{Fe}_{(12-2x)}\text{O}_{19}$ through sol–gel auto-ignition and its characterization. *J. Magn. Magn. Mater.* **2005**, *292*, 100–107. [[CrossRef](#)]
27. Shekhawat, D.; Singh, A.K.; Roy, P.K. Structural and electro-magnetic properties of high $(BH)_{\text{max}}$ La–Sm substituted Sr-hexaferrite for brushless DC electric motors application. *J. Mol. Struct.* **2019**, *1179*, 787–794. [[CrossRef](#)]
28. Eikeland, A.Z.; Stingaciu, M.; Mamakhel, A.H.; Saura-Múzquiz, M.; Christensen, M. Enhancement of magnetic properties through morphology control of $\text{SrFe}_{12}\text{O}_{19}$ nanocrystallites. *Sci. Rep.* **2018**, *8*, 7325. [[CrossRef](#)]
29. Nishio, H.; Minachi, Y.; Yamamoto, H. Effect of factors on coercivity in Sr–La–Co sintered ferrite magnets. *IEEE Trans. Magn.* **2009**, *45*, 5281–5288. [[CrossRef](#)]

Disclaimer/Publisher’s Note: The statements, opinions and data contained in all publications are solely those of the individual author(s) and contributor(s) and not of MDPI and/or the editor(s). MDPI and/or the editor(s) disclaim responsibility for any injury to people or property resulting from any ideas, methods, instructions or products referred to in the content.